Multiphonon Raman scattering mediated by the exciton states in monolayer transition metal chalcogenides

Zi-Wu Wang,* Yao Xiao, Jia-Pei Deng, Yu Cui, and Zhi-Qing Li
Tianjin Key Laboratory of Low Dimensional Materials Physics and Preparing Technology, Department of Applied Physics, School of Science, Tianjin University, Tianjin 300354 China

(Received 12 July 2019; revised manuscript received 8 September 2019; published 23 September 2019)

In the frame of Huang-Rhys's model, we study multiple orders of Raman scattering in monolayer transition metal chalcogenides (TMDC) based on the intrinsic excitons coupled with three types of phonon modes, including longitudinal optical (LO) phonon, surface optical (SO) phonon, and longitudinal acoustic (LA) phonon. We find that multiphonon structures display multiple order overtones at equal interval energies of $\hbar\omega_{\mathrm{LO}}$ and $\hbar\omega_{\mathrm{SO}}$, respectively, and intensities of overtones depend on the obtained values of Huang-Rhys factor, which can be modulated by the strength of exciton-optical phonons coupling, cutoff wave vector of optical phonon modes, and large exciton Bohr radius. Moreover, we propose the combined multiphonon processes of $p\hbar\omega_{\mathrm{LO}} + m\hbar\omega_{\mathrm{SO}}$ and $p\hbar\omega_{\mathrm{LO}}(m\hbar\omega_{\mathrm{SO}}) + \hbar\omega_{\mathrm{LA}}$. These combined processes with weaker intensity could be used to analyze the fine structure of multiphonon Raman spectra in experiments. Our theoretical results indicate that the strong exciton effect in monolayer TMDC provides an excellent platform for exploring multiphonon Raman scattering.

DOI: 10.1103/PhysRevB.100.125308

I. INTRODUCTION

Multiphonon Raman scattering (MRS) has been extensively studied in traditional II-VI and III-V semiconductor materials [1–5] and their corresponding nanostructures [6–12] during the past several decades. To explain these multiphonon processes, several theoretical models have been proposed, such as the cascade model [13], configuration coordinate model [14], and exciton-mediated state model [15]. Among them, the last one has been widely employed because it can reproduce main features of MRS in most experiments, in which bound excitons induced by the impurities and defects in samples are used for the intermediate states [2–4,6,11,12,16,17]. However, the intrinsic exciton states with very small binding energies below tens of meV are usually neglected, because they are unstable and decayed easily by thermal dissipation or scattering. Therefore, the MRS mediated by the intrinsic exciton states in traditional semiconductor materials is very hard.

As an emerging class of two-dimensional layered materials, monolayer transition metal dichalcogenides (TMDC) with the direct band gap from the visible to near-infrared spectral range, have demonstrated amounts of unique optical properties and attracted great attention in recent years [18–21]. One of the most significant properties of these monolayer materials is the strong Coulomb interaction between electrons and holes due to the reduced dimensionality and dielectric screening, which leads to the formation of strong intrinsic excitons with large binding energies in several hundreds of meV scale. This strong intrinsic exciton plays a predominant role in determining optical properties even at room temperature, which has been experimentally proved by several groups [19–21]. This opens a possible way to study MRS assisted by the intrinsic exciton states in monolayer TMDC. In fact, many recent experiments have observed the resonance Raman scattering related to exciton effect in these TMDC materials. Fan *et al.* [22] carried out a comparative resonance Raman scattering study on bulk 2H-MoS_2, WS_2, WSe_2, and monolayer MoS_2. They found that the resonance effect can be conveniently understood in terms of the excitonic excitations for these bulk materials. On the other hand, the remarkable suppression of the first-order scattering and multiphonon Raman modes in monolayer may be influenced by the substrate. Lee *et al.* [23–25] have also observed the anomalous Raman peaks in the range of 570–650 cm^{-1}, which are assigned to two-phonon resonance Raman scattering of various combined modes and can be attributed to the strong resonance with exciton or exciton polaritons. McDonnell *et al.* [26] suggested that the coupling of bright excitons and trions to large wave-vector dark states should be taken into account to analyze the multiphonon Raman peaks in their experiments. In addition, the intralayer vibrational modes E^1_{2g} and A_{1g} exhibit resonance enhancements for different exciton states in Raman scattering experiments [27,28]. In recent theoretical studies, Wang *et al.* [29] predicted the amplitudes of Raman scattering can be modulated strongly by the exciton effect based on the first-principle calculation. However, some anomalous peaks in the resonance Raman spectra cannot be explained properly and the underlying mechanisms of multiphonon scattering are ambiguous until now.

In this paper, we theoretically propose multiphonon Raman scattering assisted by the intrinsic exciton states in monolayer TMDC on the polar substrate arising from an exciton couples with the longitudinal optical (LO) phonon, surface optical (SO) phonon induced by the polar substrate, and longitudinal acoustic (LA) phonon. Multiphonon scattering for both LO and SO phonon modes are presented up to the fifth order

*wangziwu@tju.edu.cn

 ©2019 American Physical Society

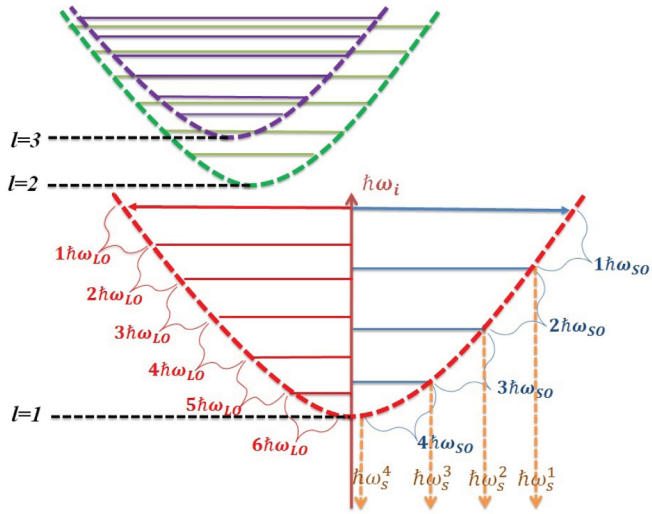

FIG. 1. The schematic diagram of multiphonon Raman scattering mediated by the exciton state. The whole process can be divided into the following steps: (1) an exciton is created by the absorption of the incident photon ($\hbar\omega_i$), (2) this exciton relaxes into lower energy states with successive emission of optical phonons ($\hbar\omega_{\rm LO}$ or $\hbar\omega_{\rm SO}$), and (3) the radiative recombination of the exciton with the emission of the scattered photon ($\hbar\omega_s^n = \hbar\omega_i - n\hbar\omega_{\rm SO(LO)}$). A series of exciton Rydberg states are denoted by the principal quantum number $l = 1, 2, \ldots$.

in the ground state of exciton. We find that multiphonon structures and the intensity of multiple order overtones depend on the obtained values of Huang-Rhys factor, which can be modulated by the radius of exciton, cutoff wave vector of optical phonon, strength of exciton-phonon coupling and internal distance between monolayer TMDC and substrates. Moreover, we propose the combined multiphonon processes of $p\hbar\omega_{\rm LO} + m\hbar\omega_{\rm SO}$ and $p\hbar\omega_{\rm LO}(m\hbar\omega_{\rm SO}) + \hbar\omega_{\rm LA}$ near the processes of $p\hbar\omega_{\rm LO}$ and $m\hbar\omega_{\rm SO}$, respectively. These combined processes with weaker intensity may be used for analyzing anomalous peaks of the Raman spectra. Finally, temperature dependences of these multiphonon Raman scattering are also discussed.

II. THEORETICAL MODEL

The strong exciton effect with a series of Rydberg states has been proved in monolayer TMDC in different experiments [19–21]. We assume an intermediate state, which consists of the exciton ground state pulsing several optical phonons, is excited by the absorption of the incident photon. Then this intermediate state relaxes into lower energy states with successive emission of optical phonons ($\hbar\omega_{\rm LO}$ or $\hbar\omega_{\rm SO}$) schemed in Fig. 1. The Raman cross section of the pth phonon process at finite temperature can be expressed as [6,12,15–17,30,31]

$$|\mathbb{R}_p|^2 = \mu_e^4 \left| \frac{\mathcal{A}_n^\nu \sum_{m=0}^{\infty} \prod_\nu \langle \chi_{g,n+p}^\nu | \chi_{e,m}^\nu \rangle \langle \chi_{e,m}^\nu | \chi_{g,n}^\nu \rangle}{E_{eg} + \sum_\nu (m-n)\hbar\omega_\nu - \hbar\omega_i + i\Gamma} \right|^2, \quad (1)$$

where μ_e is the electronic transition dipole moment, A_n^ν denotes the phonon number n for the initial vibrational levels $\chi_{g,n}^\nu$ in the ground state of exciton, m is the phonon number for the intermediate vibrational levels $\chi_{e,m}^\nu$ in the excited state of exciton. E_{eg} is the optical gap for the creation of exciton, $\hbar\omega_\nu$ is the phonon energy with νth branch (ν=LO, SO, LA), $\hbar\omega_i$ the incident photon energy, and Γ is the homogeneous linewidth of the excitonic state.

In general, MRS are calculated based on the complicated high-orders perturbation processes, which are replaced by the simple overlap integral of vibrational levels $\langle \chi_{e,m}^\nu | \chi_{g,n}^\nu \rangle$ in the Huang-Rhys's model [32,33]. Carrying out the thermal average over the initial phonon numbers and summing over all possible phonon numbers in the excited states, we converted the Raman cross section of the pth phonon process into

$$|\mathbb{R}_p|^2 = \mu_e^4 \left| \frac{\prod_\nu (\frac{\bar{n}_\nu+1}{\bar{n}_\nu})^{\frac{p}{2}} e^{-\mathcal{F}_\nu(2\bar{n}_\nu+1)} I_p(2\mathcal{F}_\nu\sqrt{\bar{n}_\nu(\bar{n}_\nu+1)})}{E_{eg} + \sum_\nu p\hbar\omega_\nu - \hbar\omega_i + i\Gamma} \right|^2, \quad (2)$$

where $\bar{n}_\nu = 1/(e^{\hbar\omega_\nu/K_BT} - 1)$ is the phonon number occupation function and K_B is the Bolzmann constant; I_p is the pth order modified Bessel function ($p = 1, 2, 3\cdots$); $\mathcal{F}_\nu$ is the Huang-Rhys (HR) factor and plays a key role in determining multiphonon processes. This factor can be calculated by

$$\mathcal{F}_\nu = \sum_k \frac{|V_\nu(k)|^2}{(\hbar\omega_\nu)^2}, \quad (3)$$

with the relaxation energy due to the exciton-phonon coupling introduced by Merlin *et al.* [17].

$$V_\nu(k) = \int \mathcal{M}_\nu(k) e^{i\mathbf{k}\cdot\mathbf{r}} \rho(\mathbf{r}) d\mathbf{r}, \quad (4)$$

where $\mathcal{M}_\nu(k)$ denotes the matrix element of exciton coupling with different phonon modes. In this paper, three types of phonon modes are taken into account and the corresponding matrix elements are [34–37]

$$\mathcal{M}_{\rm LO}(k) = \sqrt{\frac{\eta_0 L_m \hbar\omega_{\rm LO}}{2\mathbb{A}\varepsilon_0}} erfc\left(\frac{k\sigma}{2}\right), \quad (5a)$$

$$\mathcal{M}_{\rm SO}(k) = \sum_{\upsilon=1,2} \sqrt{\frac{\eta_1 \hbar\omega_{{\rm SO}_\upsilon}}{2\mathbb{A}\varepsilon_0 k}} e^{-kz_0}, \quad (5b)$$

$$\mathcal{M}_{\rm LA}(k) = i\sqrt{\frac{D^2\hbar k}{2\mathbb{A}\varrho\omega_{\rm LA}}} erfc\left(\frac{k\sigma}{2}\right), \quad (5c)$$

for LO, SO, and LA phonon modes, respectively. Here the polarization parameter η_0 (η_1) reflects the strength of exciton-LO (-SO) coupling quantitatively, L_m is the thickness of monolayer TMDC, $\mathbb{A}$ is the quantization area in the monolayer plane and ε_0 is the permittivity of free space, $erfc(k\sigma/2)$ is the complementary error function, in which σ is the effective width of the electronic Bloch states, z_0 is the internal distance between monolayer TMDC and substrate, ϱ is the mass density, D denotes the deformation potential constant, and $\omega_{\rm LA}$ is the LA phonon frequency.

In Eq. (4), the electronic charge density $\rho(\mathbf{r})$ consisting of a hole and an electron in the hydrogenic model is adopted the same as these previous studies [6,12,16,17]

$$\rho(\mathbf{r}) = \rho_h(\mathbf{r}) + \rho_e(\mathbf{r}), \quad (6a)$$

TABLE I. Two branches of surface optical phonon modes are induced by the polar substrate. Only one branch with small energies are illustrated. Parameters are the same as in Refs. [35,36].

Quantity (units)	h-BN	SiO_2	Al_2O_3
η_1	0.032	0.082	0.164
$\hbar\omega_{\rm SO}$ (meV)	101	60	55

with

$$\rho_h(\mathbf{r}) = \mathbf{e}\delta(\mathbf{r}), \tag{6b}$$

and

$$\rho_e(\mathbf{r}) = -\mathbf{e}|\psi_{1s}(\mathbf{r})|^2 = -\mathbf{e}\left(\frac{2}{\pi a_B^2}\right)e^{-\frac{2r}{a_B}}, \tag{6c}$$

where $\mathbf{e}$ is the charge carrier and $\psi_{1s}(\mathbf{r})$ is the exciton ground state with the Bohr radius a_B [38–40]. Performing the integral for Eq. (4), one can get

$$V_\nu(k) = \mathcal{M}_\nu(k)\left[1 - \frac{8}{\left(4 + k^2 a_B^2\right)^{3/2}}\right]. \tag{7}$$

Substituting Eq. (7) into Eq. (4) and converting the summation of wave vector k into integral, one can write the HR factor as

$$\begin{aligned}\mathcal{F}_\nu &= \sum_k \left|\frac{\mathcal{M}_\nu(k)}{\hbar\omega_\nu}\right|^2\left[1 - \frac{8}{\left(4 + k^2 a_B^2\right)^{3/2}}\right]^2 \\ &= \frac{\mathbb{A}}{(2\pi)^2}\int_0^{k_c}\left|\frac{\mathcal{M}_\nu(k)}{\hbar\omega_\nu}\right|^2\left[1 - \frac{8}{\left(4 + k^2 a_B^2\right)^{3/2}}\right]^2 k dk,\end{aligned} \tag{8}$$

where k_c is the cutoff wave vector of νth phonon modes. According to the matrix elements in Eqs. (5a)–(5c), HR factors for LO, SO, LA phonon modes in Eq. (8) are calculated numerically.

In fact, Eq. (2) can be expanded to study many types of MRS processes. We only focus on four types of multiphonon processes $p\hbar\omega_{\rm LO}$, $m\hbar\omega_{\rm SO}$, $p\hbar\omega_{\rm LO}(m\hbar\omega_{\rm SO}) + \hbar\omega_{\rm LA}$, and $p\hbar\omega_{\rm LO} + m\hbar\omega_{\rm SO}$ in the present paper, the corresponding Raman cross sections are

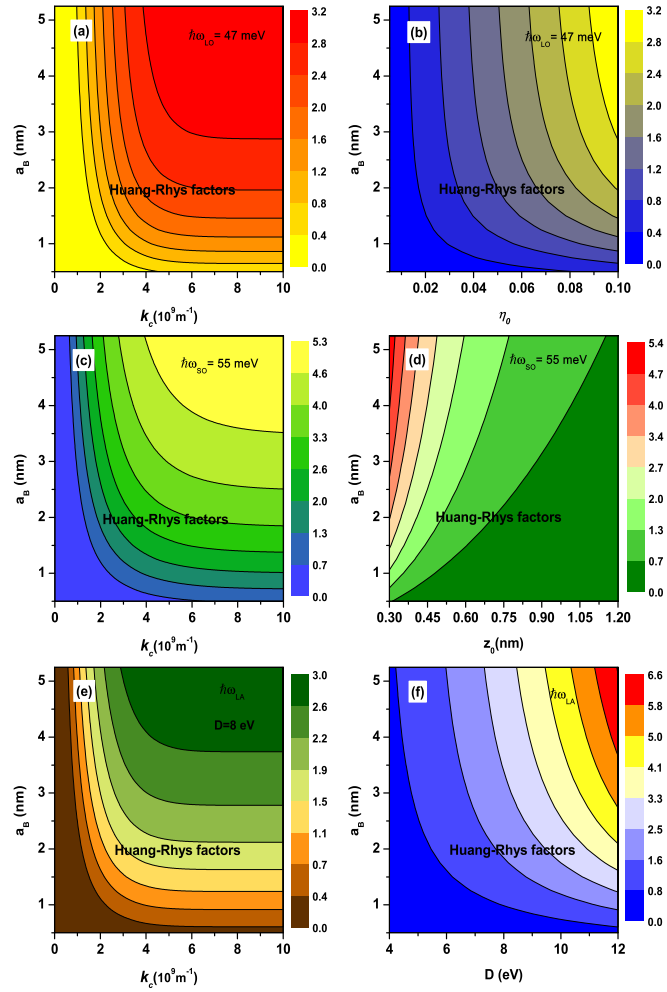

FIG. 2. (a) Huang-Rhys (HR) factor of the LO phonon mode as functions of the exciton Bohr radius (a_B) and cutoff wave vectors k_c at the polarization parameter $\eta_0 = 0.1$ in monolayer MoS_2. (b) HR factor of the LO phonon mode as functions of a_B and η_0. (c) The dependences of HR factor on a_B and k_c for the SO phonon mode in monolayer MoS_2 on Al_2O_3 substrate at the internal distance $z_0 = 0.3$ nm. (d) The dependences of HR factor on a_B and z_0 for the SO phonon mode. (e) The relations of HR factor with a_B and k_c for the LA phonon mode at fixed deformation potential constant $D = 8$ eV. (f) The relations of HR factor with a_B and D for the LA phonon mode.

$$|\mathbb{R}_{p\hbar\omega_{\rm LO}}|^2 = \mu_e^4\left|\frac{\left(\frac{\bar{n}_{\rm LO}+1}{\bar{n}_{\rm LO}}\right)^{\frac{p}{2}} e^{-\mathcal{F}_{\rm LO}(2\bar{n}_{\rm LO}+1)} I_p\left(2\mathcal{F}_{\rm LO}\sqrt{\bar{n}_{\rm LO}(\bar{n}_{\rm LO}+1)}\right)}{E_{eg} + p\hbar\omega_{\rm LO} - \hbar\omega_i + i\Gamma}\right|^2, \tag{9}$$

$$|\mathbb{R}_{m\hbar\omega_{\rm SO}}|^2 = \mu_e^4\left|\frac{\left(\frac{\bar{n}_{\rm SO}+1}{\bar{n}_{\rm SO}}\right)^{\frac{m}{2}} e^{-\mathcal{F}_{\rm SO}(2\bar{n}_{\rm SO}+1)} I_m\left(2\mathcal{F}_{\rm SO}\sqrt{\bar{n}_{\rm SO}(\bar{n}_{\rm SO}+1)}\right)}{E_{eg} + m\hbar\omega_{\rm SO} - \hbar\omega_i + i\Gamma}\right|^2, \tag{10}$$

$$|\mathbb{R}_{p\hbar\omega_{\lambda={\rm LO,SO}}+\hbar\omega_{\rm LA}}|^2 = \mu_e^4\left|\frac{\left(\frac{\bar{n}_\lambda+1}{\bar{n}_\lambda}\right)^{\frac{p}{2}} e^{-\mathcal{F}_\lambda(2\bar{n}_\lambda+1)} I_p\left(2\mathcal{F}_\lambda\sqrt{\bar{n}_\lambda(\bar{n}_\lambda+1)}\right)\left(\frac{\bar{n}_{\rm LA}+1}{\bar{n}_{\rm LA}}\right)^{\frac{1}{2}} e^{-\mathcal{F}_{\rm LA}(2\bar{n}_{\rm LA}+1)} I_1\left(2\mathcal{F}_{\rm LA}\sqrt{\bar{n}_{\rm LA}(\bar{n}_{\rm LA}+1)}\right)}{E_{eg} + p\hbar\omega_\lambda + \hbar\omega_{\rm LA} - \hbar\omega_i + i\Gamma}\right|^2, \tag{11}$$

$$|\mathbb{R}_{p\hbar\omega_{\rm LO}+m\hbar\omega_{\rm SO}}|^2 = \mu_e^4\left|\frac{\left(\frac{\bar{n}_{\rm LO}+1}{\bar{n}_{\rm LO}}\right)^{\frac{p}{2}} e^{-\mathcal{F}_{\rm LO}(2\bar{n}_{\rm LO}+1)} I_p\left(2\mathcal{F}_{\rm LO}\sqrt{\bar{n}_{\rm LO}(\bar{n}_{\rm LO}+1)}\right)\left(\frac{\bar{n}_{\rm SO}+1}{\bar{n}_{\rm SO}}\right)^{\frac{m}{2}} e^{-\mathcal{F}_{\rm SO}(2\bar{n}_{\rm SO}+1)} I_m\left(2\mathcal{F}_{\rm SO}\sqrt{\bar{n}_{\rm SO}(\bar{n}_{\rm SO}+1)}\right)}{E_{eg} + p\hbar\omega_{\rm LO} + m\hbar\omega_{\rm SO} - \hbar\omega_i + i\Gamma}\right|^2. \tag{12}$$

In the numerical calculation processes, we select the structure of monolayer MoS_2 laying on polar substrate as an example to discuss MRS. The parameters for the monolayer MoS_2 are listed as following [34,37]: $\hbar\omega_{\rm LO} = 47$ meV, $L_m = 0.44$ nm, $\sigma = 0.64$ nm, the LA phonon modes with the linear dispersion $\omega_{\rm LA} = c\,k$ ($c = 0.64 \times 10^3$ m/s). Throughout this paper, the broadening factor $\Gamma = 5$ meV is assumed. The SO phonon mode with the single frequency and the corresponding parameters have been listed in Table I. In addition, the intrinsic exciton states are divided into A and B types due to the strong spin-orbit splitting [20,21]. We only study multiphonon scattering mediated by A exciton and assume that B exciton has the similar effect.

III. RESULTS AND DISCUSSION

The exciton state is dressed by the "phonon cloud" due to the strong exciton-phonon coupling. The energy of the "phonon cloud," that is the lattice relaxation energy, is described by $\mathcal{F}_\nu\hbar\omega_\nu$ and varies with different exciton states in the Huang-Rhys's model, in which HR factor $\mathcal{F}_\nu$ reflects the average phonon numbers of νth mode around the exciton. Figure 2 presents the variation of HR factors of LO, SO, and LA phonon modes in the exciton ground state in monolayer MoS_2 on Al_2O_3 substrate. The dependences of HR factors on the exciton Bohr radius (a_B) and cutoff wave vector of phonon modes (k_c) are shown in Figs. 2(a), 2(c), and 2(e) for LO, SO, and LA phonon modes, respectively. One can see that HR factors increase with increasing k_c. But the influence of k_c on HR factors becomes insignificant as k_c exceeds the value of $6 \times 10^9/m$. This indicates that only the phonon modes with the small wave vector, corresponding to the long wavelength phonons, are strongly coupled with the exciton, which is consistent with the first-principle calculation results that small-momentum optical phonons give the predominate contributions to the Fröhlich interaction [41,42]. On the other hand, HR factors increase obviously with increasing a_B. The reasons are that (1) an exciton is similar to an electric dipole, and thus the larger a_B, the bigger electric dipole moment; (2) the exciton-phonon coupling can be regarded as an electric dipole coupling with the phonon field, so the enlargement of a_B results in the enhancement of exciton-phonon coupling. The effective exciton Bohr radius of the monolayer TMDC was predicted on the order of 1 nm in different theoretical calculations [20,21]. However, the experimental results [43–45] indicate that the effective values are several times larger than the theoretical ones. That is why the values of a_B are settled in a large scale in the present model. Figure 2(b) shows that the big values of $\mathcal{F}_{\rm LO}$ can be obtained as the polarization parameter (η_0) increases. This is because η_0 reflects the strength of carrier-LO phonon coupling directly for these monolayer TMDC materials given in Eq. 5(a). Several

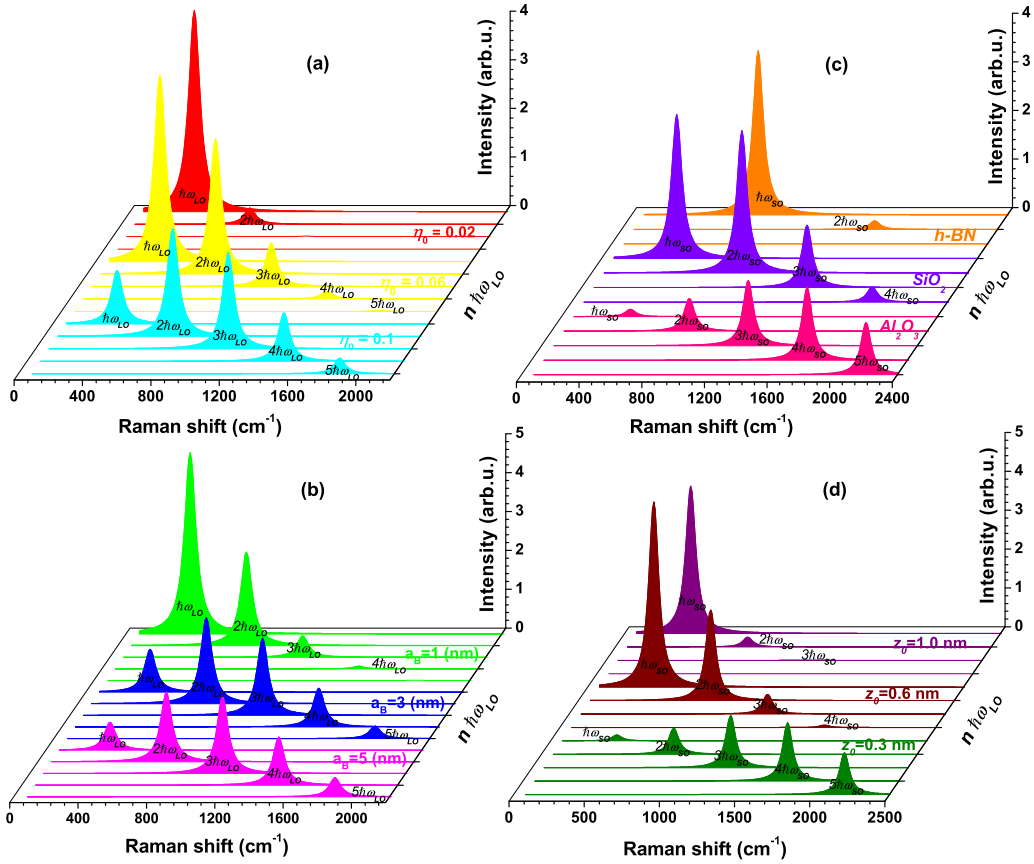

FIG. 3. (a) Multiple LO phonons Raman scattering for different polarization parameters at $a_B = 3$ nm. (b) Multiple LO phonons Raman scattering for different exciton Bohr radius at $\eta_0 = 0.1$ nm. (c) Multiple SO phonons Raman scattering in monolayer MoS_2 laying on different polar substrates at $a_B = 3$ nm and at $z_0 = 0.3$ nm. (d) Multiple SO phonons Raman scattering in monolayer MoS_2 on Al_2O_3 substrate at different internal distances and at $a_B = 3$ nm.

recent studies [35,41,42] have also pointed out that carriers-LO phonon coupling in monolayer TMDC is much stronger than that in previous studies. A new parameter g_F was defined as the coupling strength, which is analogous to the parameter η_0 and can be tuned in the wide range. Nevertheless, the quantitative comparisons between η_0 and g_F are still lacking. The SO phonon modes are induced by the supporting substrate, which determines the decay of carrier-SO phonon coupling following the exponential trend with the internal distance presented in Eq. 5(b), and thus $\mathcal{F}_{\rm SO}$ decreases sharply with the internal distance shown in Fig. 2(d). Figure 2(f) shows the dependence of $\mathcal{F}_{\rm LA}$ on the deformation potential constants. One can see that $\mathcal{F}_{\rm LA}$ increases significantly with the deformation potential constant because this constant is related directly to the strength of exciton-LA phonon coupling in the deformation potential mechanism. From Fig. 2, we conclude that large enough values of $\mathcal{F}_{\rm LO}$, $\mathcal{F}_{\rm SO}$, and $\mathcal{F}_{\rm LA}$ in the excitonic ground state are obtained theoretically at some certain conditions. These large HR factors ensure the exciton with sufficient energy (or average phonon numbers around it) to relax via the successive emission of optical phonons.

According to Eqs. (9) and (10), MRS for LO and SO phonon modes intermediated by the exciton ground state are shown in Fig. 3 at temperature $T = 77$ K. From Fig. 3(a), one can see that overtone of the LO phonon mode only steps up to the second order at $\eta_0 = 0.02$. However, it can step up to fourth and fifth orders as $\eta_0 = 0.06, 0.1$, respectively. This is attributed to the dependence of $\mathcal{F}_{\rm LO}$ on η_0 shown in Fig. 2(b). Anther remarkable feature is that intensities of overtones exhibit a linear decay from the first to the higher orders at $\eta_0 = 0.02$ and 0.06. But the intensities of overtones follow an asymmetric Gaussian distribution and the maximum intensity shifts to the second order overtone at $\eta_0 = 0.1$. Two types of variational trend for the intensity of overtone are in good agreement with the previous measurements in multiphonon Raman experiments for traditional II-VI and III-V semiconductor materials [4,6,12]. We give the explanations that (1) the values of $\mathcal{F}_{\rm LO}$ are in the range of $0 \sim 1.8$ for both $\eta_0 = 0.02$ and $\eta_0 = 0.06$ at $a_B \leqslant 3$ nm shown in Fig. 2(b). This means that the Raman process via one LO phonon scattering is the maximum probability issue. (2) When $\eta_0 = 0.1$, HR factor satisfies the relation of $2 \leqslant \mathcal{F}_{\rm LO} < 3$, which gives rise to two-LO phonon scattering (the second order overtone) becomes the maximum probability issue in the Raman processes. It is therefore concluded that the pth order overtone in multiple LO phonon Raman scattering will reach to the maximum intensity as the condition of $p \leqslant \mathcal{F}_{\rm LO} < p+1$ is satisfied. This result needs to be confirmed in future experiments. Figure 3(b) shows influence of a_B on the multiple LO phonons Raman scattering. The similar variational trend for the intensity of overtone is obtained as concluded in Fig. 3(a), which can be traced back to the dependence of $\mathcal{F}_{\rm LO}$ on a_B given in Fig. 2. Multiple SO phonons Raman scattering on three types of polar substrates are plotted in Fig. 3(c) at $z_0 = 0.3$ nm. From it, one can see that both intensity and orders of overtones vary for different polar substrates. These variations arise from the strength of exciton-SO phonon coupling depending on the polarizability of substrate that is reflected by the parameter η' given in Table I. The obvious modulation effects of z_0 on multiple SO phonons Raman scattering are presented in Fig. 3(d). Hence, differing from multiple LO phonons Raman scattering, the SO phonon scattering can be tuned by choosing polar substrates and changing internal distance, which could be carried out in practical experiments.

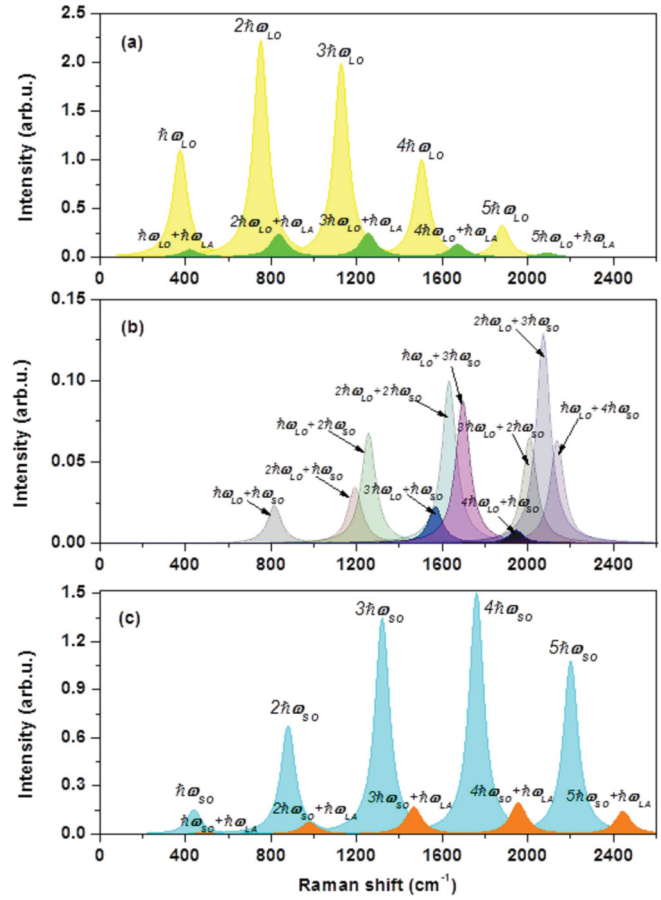

FIG. 4. In the structure of MoS_2/Al_2O_3, (a) multiphonon Raman scattering (MRS) of $p\hbar\omega_{\rm LO}$ and combined $p\hbar\omega_{\rm LO} + \hbar\omega_{\rm LA}$ processes, (b) MRS of the combined $p\hbar\omega_{\rm LO}$+$m\hbar\omega_{\rm LO}$ processes, and (c) MRS of $m\hbar\omega_{\rm SO}$ and combined $m\hbar\omega_{\rm SO} + \hbar\omega_{\rm LA}$ processes, where several parameters $D = 8$ eV, $\eta_0 = 0.1$, $T = 77$ K, and $z_0 = 0.3$ nm are fixed.

An advantage of the Huang-Rhys model for multiphonon scattering is that it gives many types of combined multiphonon processes described in Eqs. (11) and (12). Figure 4(a) shows MRS of $p\hbar\omega_{\rm LO}$ and combined $p\hbar\omega_{\rm LO} + \hbar\omega_{\rm LA}$ processes. From the comparison, one can find that (1) intensities of the combined $p\hbar\omega_{\rm LO} + \hbar\omega_{\rm LA}$ processes are weaker than the processes of $p\hbar\omega_{\rm LO}$ due to the combination of scattering probability for different phonon modes; (2) the changing trends of intensity for two types of multiphonon processes are similar. These combined processes of $p\hbar\omega_{\rm LO} + \hbar\omega_{\rm LA}$ may be proven as the abnormal shoulders of MRS of LO phonon mode in experiments [25,46–48]. MRS of $m\hbar\omega_{\rm SO}$ and combined $m\hbar\omega_{\rm SO} + \hbar\omega_{\rm LA}$ processes are also shown in Fig. 4(c). The results are similar to that of Fig. 4(a). According to Eq. (12), many possible multiphonon scattering of $p\hbar\omega_{\rm LO}$+$m\hbar\omega_{\rm SO}$ based on the combination of LO with SO phonon modes are presented in Fig. 4(b). These combined processes with weaker intensity locate between $p\hbar\omega_{\rm LO}$ ($m\hbar\omega_{\rm SO}$) and $(p+1)\hbar\omega_{\rm LO}$

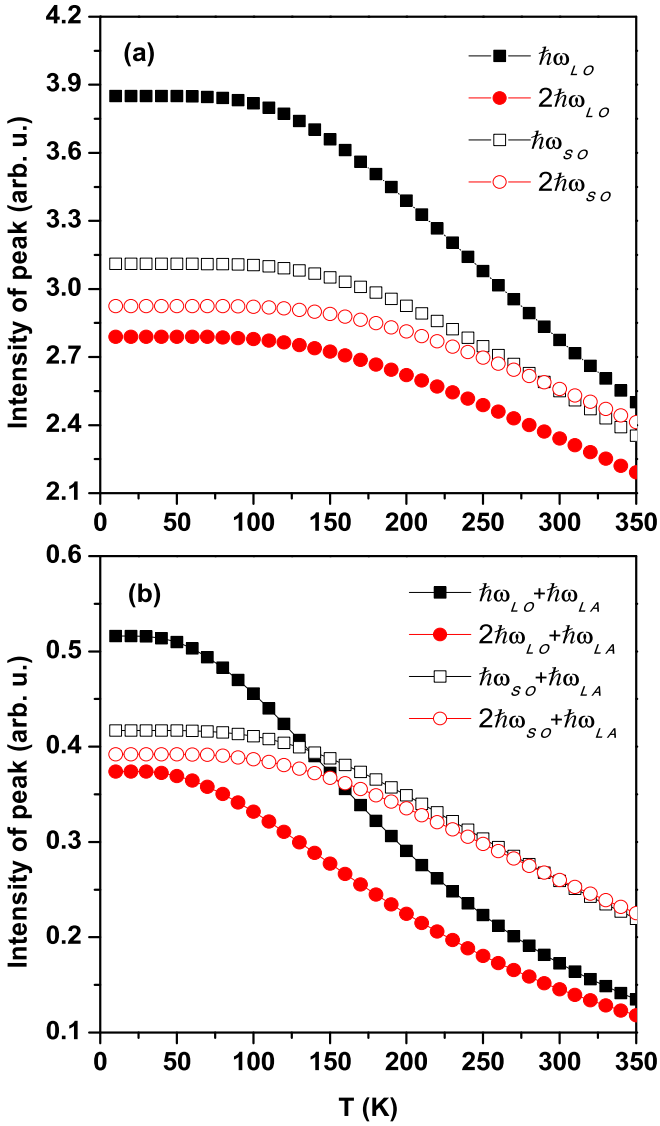

FIG. 5. (a) Intensity of peaks for the processes of $\hbar\omega_{\rm SO}$ ($\hbar\omega_{\rm LO}$) and $2\hbar\omega_{\rm SO}$ ($2\hbar\omega_{\rm LO}$) as a function of temperature. (b) Intensity of peaks for the combined processes of $\hbar\omega_{\rm SO}+\hbar\omega_{\rm LA}$ ($\hbar\omega_{\rm LO}+\hbar\omega_{\rm LA}$) and $2\hbar\omega_{\rm SO}+\hbar\omega_{\rm LA}$ ($2\hbar\omega_{\rm LO}+\hbar\omega_{\rm LA}$) as a function of temperature in monolayer MoS_2 on Al_2O_3 substrate, where several parameters $D=8$ eV, $\eta_0=0.1$, and $z_0=0.3$ nm are fixed.

$((m+1)\hbar\omega_{\rm SO})$ processes, which are useful for analyzing of the fine structures in multiphonon Raman spectra. In addition, many other combined multiphonon processes, such as $m\hbar\omega_{\rm SO}+p\hbar\omega_{\rm LA}$, $p\hbar\omega_{\rm LO}+m\hbar\omega_{\rm LA}$, and $p\hbar\omega_{\rm LO}+m\hbar\omega_{\rm SO}+\hbar\omega_{\rm LA}$ can be also given in this model if necessary for the analysis of fine structures in Raman spectra.

The processes of $\hbar\omega_{\rm SO}$ ($\hbar\omega_{\rm LO}$) and $2\hbar\omega_{\rm SO}$ ($2\hbar\omega_{\rm LO}$) as well as the combined processes of $\hbar\omega_{\rm SO}+\hbar\omega_{\rm LA}$ ($\hbar\omega_{\rm LO}+\hbar\omega_{\rm LA}$) and $2\hbar\omega_{\rm SO}+\hbar\omega_{\rm LA}$ ($2\hbar\omega_{\rm LO}+\hbar\omega_{\rm LA}$) are selected as examples to discuss the temperature dependence of MRS in Fig. 5. One can find that intensities of their peaks vary smoothly in low temperature regime, and then decrease at certain temperature, which can be called as the temperature turning point, depending on the energies of phonon modes. The temperature turning points of the combined processes in Fig. 5(b) are smaller than that of the processes in Fig. 5(a). This stems from the combined processes including the LA phonon modes that are motivated more easier than LO phonon modes. Moreover, the temperature dependences of the intensity of MRS are consistent with the experimental measurements in traditional semiconductor materials [9,10] and need to be confirmed in the following experiments for these monolayer TMDS materials.

IV. CONCLUSIONS

In conclusion, we theoretically study multiphonon Raman scattering (MRS) in monolayer TMDC on different polar substrates. We find that (i) the maximum intensity of the pth order overtone for optical phonon modes appears at the condition of $p\leqslant\mathcal{F}_{\lambda=\rm LO,SO}<p+1$, depending on the modulation of HR factors $\mathcal{F}_{\lambda=\rm LO,SO}$ by several parameters, such as exciton Bohr radius, polarizibilty of substrate and internal distance; (ii) the combined multiphonon processes with weaker intensity could be used to analyze these abnormal peaks in multiphonon Raman spectra; (iii) the predicted temperature dependences of MRS in these monolayer TMDC are in good agreement with the previous experimental results in traditional semiconductor materials.

ACKNOWLEDGMENT

This work was supported by National Natural Science Foundation of China (Grant No. 11674241).

[1] J. F. Scott, uv resonant raman scattering in ZnO, Phys. Rev. B **2**, 1209 (1970).
[2] W. H. Sun, S. J. Chua, L. S. Wang, and X. H. Zhang, Outgoing multiphonon resonant Raman scattering and luminescence in Be- and C-implanted GaN, J. Appl. Phys. **91**, 4917 (2002).
[3] J. W. Ager, W. Walukiewicz, W. Shan, K. M. Yu, S. X. Li, E. E. Haller, H. Lu, and W. J. Schaff, Multiphonon resonance Raman scattering in $In_xGa_{1-x}N$, Phys. Rev. B **72**, 155204 (2005).
[4] X. Zhu, H. Wu, Z. Yuan, J. Kong, and W. Shen, Multiphonon resonant Raman scattering in N-doped ZnO, J. Raman Spectrosc. **40**, 2155 (2009).
[5] M. Kumar, M. Becker, T. Wernicke, and R. Singh, Multiphonon resonant Raman scattering in non-polar GaN epilayer, Appl. Phys. Lett. **105**, 142106 (2014).
[6] M. C. Klein, F. Hache, D. Ricard, and C. Flytzanis, Size dependence of electron-phonon coupling in semiconductor nanospheres: The case of CdSe, Phys. Rev. B **42**, 11123 (1990).
[7] E. P. Pokatilov, S. N. Klimin, V. M. Fomin, J. T. Devreese, and F. W. Wise, Multiphonon Raman scattering in semiconductor nanocrystals: Importance of nonadiabatic transitions, Phys. Rev. B **65**, 075316 (2002).
[8] C. Trallero-Giner, F. de Leon-Pérez, M. Lu, and J. L. Birman, Scattering of hot excitons due to optical phonons in quantum

wells: Multiphonon resonant Raman process, Phys. Rev. B **65**, 115314 (2002).

[9] Y. Viale, P. Gilliot, O. Crëgut, J.-P. Likforman, M. Gallart, B. Hönerlage, K. Kheng, and H. Mariette, Scattering of hot excitons due to optical phonons in quantum wells: Multiphonon resonant Raman process, Phys. Rev. B **69**, 115324 (2004).

[10] V. V. Ursaki, I. M. Tiginyanu, V. V. Zalamai, E. V. Rusu, G. A. Emelchenko, V. M. Masalov, and E. N. Samarov, Multiphonon resonant Raman scattering in ZnO crystals and nanostructured layers, Phys. Rev. B **70**, 155204 (2004).

[11] C. Singh and S. Rath, Spectroscopic ellipsometry and multiphonon Raman spectroscopic study of excitonic effects in ZnO films, J. Appl. Phys. **113**, 163104 (2013).

[12] Q. Zhang, J. Zhang, M. I. B. Utama, B. Peng, M. delaMata, J. Arbiol, and Q. Xiong, Exciton-phonon coupling in individual ZnTe nanorods studied by resonant Raman spectroscopy, Phys. Rev. B **85**, 085418 (2012).

[13] R. M. Martin and C. M. Varma, Cascade Theory of Inelastic Csattering of Light, Phys. Rev. Lett. **26**, 1241 (1971).

[14] M. L. Wilimas and J. Smit, Multiple-phonon resonance Raman scattering theory, Solid State Commun. **8**, 2009 (1970).

[15] E. Mulazzi, Raman Scattering in Resonance with the Exciton Transition in Prue Polar Crystals, Phys. Rev. Lett. **25**, 228 (1970).

[16] T. P. Martin and S. Onari, Multiple-order Raman scattering in MnO_4^{2-}-doped CsI, Phys. Rev. B **15**, 1093 (1977).

[17] R. Merlin, G. Güntherodt, R. Humphreys, M. Cardona, R. Suryanarayanan, and F. Holtzberg, Multiphonon processes in YbS, Phys. Rev. B **17**, 4951 (1978).

[18] H. Yu, X. Cui, X. Xu, and W. Yao, Valley excitons in two-dimensional semiconductors, Natl. Sci. Rev. **2**, 57 (2015).

[19] J. Xiao, M. Zhao, Y. Wang, and X. Zhang, Excitons in atomically thin 2D semiconductors and their applications, Nanophotonics **6**, 1309 (2017).

[20] T. C. Berkelbach and D. R. Reichman, Optical and excitonic properties of atomically thin transition-metal dichalcogenides, Annu. Rev. Condens. Matter Phys. **9**, 379 (2018).

[21] G. Wang, A. Chernikov, M. M. Glazov, T. F. Heinz, X. Marie, T. Amand, and B. Urbaszek, Excitons in atomically thin transition metal dichalcogenides, Rev. Mod. Phys. **90**, 021001 (2018).

[22] J. H. Fan, P. Gao, A. M. Zhang, B. R. Zhu, H. L. Zeng, X. D. Cui, R. He, and Q. M. Zhang, Resonance Raman scattering in bulk 2H-MX_2 (M=Mo, W; X=S, Se) and monolayer MoS_2, J. Appl. Phys. **115**, 053527 (2014).

[23] J. U. Lee, J. Park, Y. W. Sonb, and H. Cheong, Anomalous excitonic resonance Raman effects in few-layered MoS_2, Nanoscale **7**, 3229 (2015).

[24] J. U. Lee, K. Kim, and H. Cheong, Resonant Raman and photoluminescence spectra of suspended molybdenum disulfide, 2D Mater. **2**, 044003 (2015).

[25] J. U. Lee and H. Cheong, Resonance Raman effects in transition metal dichalcogenides, J. Raman Spectrosc. **49**, 66 (2018).

[26] L. P. McDonnell, C. C. Huang, Q. Cui, D. W. Hewak, and D. C. Smith, Probing excitons, trions and dark excitons in monolayer WS_2 using resonance Raman spectroscopy, Nano Lett. **18**, 1428 (2018).

[27] B. R. Carvalho, L. M. Malard, J. M. Alves, C. Fantini, and M. A. Pimenta, Symmetry-Dependent Exciton-Phonon Coupling in 2D and Bulk MoS_2 Observed by Resonance Raman Scattering, Phys. Rev. Lett. **114**, 136403 (2015).

[28] P. Soubelet, A. E. Bruchhausen, A. Fainstein, K. Nogajewski, and C. Faugeras, Resonance effects in the Raman scattering of monolayer and few-layer $MoSe_2$, Phys. Rev. B **93**, 155407 (2016).

[29] Y. Wang, B. R. Carvalho, and V. H. Crespi, Strong exciton regulation of Raman scattering in monolayer MoS_2, Phys. Rev. B **98**, 161405(R) (2018).

[30] A. C. Albrecht, On the theory of Raman intensities, J. Chem. Phys. **34**, 1476 (1961).

[31] A. P. Alivisatos, T. D. Harris, P. J. Carroll, M. L. Steigerwald, and L. E. Brus, Electron-vibration coupling in semiconductor clusters studied by resonance Raman spectroscopy, J. Chem. Phys. **90**, 3463 (1989).

[32] K. Huang and A. Rhys, Theory of light absorption and nonradiative transitions in F-centres, Proc. Roy. Soc. A **204**, 406 (1950).

[33] K. Huang, Adiabatic approximation theory and static coupling theory of nonradiative transition, Scientia Sinica **24**, 27 (1981).

[34] K. Kaasbjerg, K. S. Thygesen, and K. W. Jacobsen, Phonon-limited mobility in n-type single-layer MoS_2 from first principles, Phys. Rev. B **85**, 115317 (2012).

[35] B. Scharf, V. Perebeinos, J. Fabian, and P. Avouris, Effects of optical and surface polar phonons on the optical conductivity of doped graphene, Phys. Rev. B **87**, 035414 (2013).

[36] C. V. Nguyen, N. N. Hieu, N. A. Poklonski, V. V. Ilyasov, L. Dinh, T. C. Phong, L. V. Tung, and H. V. Phuc, Magneto-optical transport properties of monolayer MoS_2 on polar substrates, Phys. Rev. B **96**, 125411 (2017).

[37] K. Kaasbjerg, K. S. Bhargavi, and S. S. Kubakaddi, Hot-electron cooling by acoustic and optical phonons in monolayers of MoS_2 and other transition-metal dichalcogenides, Phys. Rev. B **90**, 165436 (2014).

[38] K. L. He, N. Kumar, L. Zhao, Z. F. Wang, K. F. Mak, H. Zhao, and J. Shan, Tightly Bound Excitons in Monolayer WSe_2, Phys. Rev. Lett. **113**, 026803 (2014).

[39] A. Chernikov, T. C. Berkelbach, H. M. Hill, A. Rigosi, Y. L. Li, O. B. Aslan, D. R. Reichman, M. S. Hybertsen, and T. F. Heinz, Exciton Binding Energy and Nonhydrogenic Rydberg Series in Monolayer WS_2, Phys. Rev. Lett. **113**, 076802 (2014).

[40] T. Olsen, S. Latini, F. Rasmussen, and K. S. Thygesen, Simple Screened Hydrogen Model of Excitons in Twodimensional Materials, Phys. Rev. Lett. **116**, 056401 (2016).

[41] T. Sohier, M. Calandra, and F. Mauri, Two-dimensional Fröhlich interaction in transition-metal dichalcogenide monolayers: Theoretical modeling and first-principles calculations, Phys. Rev. B **94**, 085415 (2016).

[42] D. V. Tuan, B. Scharf, Z. Wang, J. Shan, K. F. Mak, I. Žutić, and H. Dery, Probing many-body interactions in monolayer transition-metal dichalcogenides, Phys. Rev. B **99**, 085301 (2019).

[43] A. V. Stier, N. P. Wilson, G. Clark, X. Xu, and S. A. Crooker, Probing the influence of dielectric environment on excitons in monolayer WSe_2: Insight from high magnetic fields, Nano Lett. **16**, 7054 (2016).

[44] A. V. Stier, N. P. Wilson, K. A. Velizhanin, J. Kono, X. Xu, and S. A. Crooker, Magnetooptics of Exciton Rydberg States

in a Monolayer Semiconductor, Phys. Rev. Lett. **120**, 057405 (2018).

[45] B. Han, C. Robert, E. Courtade, M. Manca, S. Shree, T. Amand, P. Renucci, T. Taniguchi, K. Watanabe, X. Marie, L. E. Golub, M. M. Glazov, and B. Urbaszek, Exciton States in Monolayer $MoSe_2$ and $MoTe_2$ Probed by Upconversion Spectroscopy, Phys. Rev. X **8**, 031073 (2018).

[46] W. Zhao, Z. Ghorannevis, K. K. Amara, J. R. Pang, M. Toh, X. Zhang, C. Kloc, P. H. Tan, and G. Eda, Lattice dynamics in mono- and few-layer sheets of WS_2 and WSe_2, Nanoscale **5**, 9677 (2013).

[47] K. Golasa, M. Grzeszczyk, P. Leszczynski, C. Faugeras, A. A. L. Nicolet, A. Wysmoek, M. Potemski, and A. Babinski, Multiphonon resonant Raman scattering in MoS_2, Appl. Phys. Lett. **104**, 092106 (2014).

[48] T. Livneh and J. E. Spanier, A comprehensive multiphonon spectral analysis in MoS_2, 2D Mater. **2**, 035003 (2015).